

Current constrained voltage scaled reconstruction (CCVSR) algorithm for MR-EIT and its performance with different probing current patterns

To cite this article: Özlem Birgül *et al* 2003 *Phys. Med. Biol.* **48** 653

View the [article online](#) for updates and enhancements.

Related content

- [Equipotential projection for MR-EIT](#)
Mahir S Özdemir, B Murat Eyübolu and Orçun Özbek
- [Experimental results for MR-EIT](#)
Özlem Birgül, B Murat Eyübolu and Y Ziya İder
- [Three-dimensional forward solver for MREIT](#)
Byung Il Lee, Suk Hoon Oh, Eung Je Woo *et al.*

Recent citations

- [A harmonic -based conductivity reconstruction method in MREIT with influence of non-transversal current density](#)
Kiwon Jeon *et al*
- [Two alternatives for magnetic resonance electrical impedance tomography: injected or induced current](#)
Hasan H Eroglu and B Murat Eyübolu
- [Single acquisition electrical property mapping based on relative coil sensitivities: A proof-of-concept demonstration](#)
José *et al*



**TURN UNCERTAINTY
INTO PEACE OF MIND**

Get ready for Beam Commissioning 4.0



Current constrained voltage scaled reconstruction (CCVSR) algorithm for MR-EIT and its performance with different probing current patterns

Özlem Birgül¹, B Murat Eyüboğlu¹ and Y Ziya İder²

¹ Department of Electrical and Electronics Engineering, Middle East Technical University, 06531 Ankara, Turkey

² Department of Electrical and Electronics Engineering, Bilkent University, 06533 Ankara, Turkey

E-mail: meyub@metu.edu.tr

Received 18 September 2002, in final form 8 January 2003

Published 18 February 2003

Online at stacks.iop.org/PMB/48/653

Abstract

Conventional injected-current electrical impedance tomography (EIT) and magnetic resonance imaging (MRI) techniques can be combined to reconstruct high resolution true conductivity images. The magnetic flux density distribution generated by the internal current density distribution is extracted from MR phase images. This information is used to form a fine detailed conductivity image using an Ohm's law based update equation. The reconstructed conductivity image is assumed to differ from the true image by a scale factor. EIT surface potential measurements are then used to scale the reconstructed image in order to find the true conductivity values. This process is iterated until a stopping criterion is met. Several simulations are carried out for opposite and cosine current injection patterns to select the best current injection pattern for a 2D thorax model. The contrast resolution and accuracy of the proposed algorithm are also studied. In all simulation studies, realistic noise models for voltage and magnetic flux density measurements are used. It is shown that, in contrast to the conventional EIT techniques, the proposed method has the capability of reconstructing conductivity images with uniform and high spatial resolution. The spatial resolution is limited by the larger element size of the finite element mesh and twice the magnetic resonance image pixel size.

1. Introduction

Knowledge of the *in vivo* conductivity distribution in the human body is vital in many biomedical applications. Accurate conductivity images can be used in monitoring physiological functions (Frerichs 2000, Morucci and Rigaud 1996) and it has been proved

that information about *in vivo* tissue conductivity values improves the solution accuracy of bioelectrical field problems (Van Burik and Peters 2000, Gonçalves *et al* 2000). In the late seventies, electrical impedance tomography (EIT) was proposed to provide this information (Boone *et al* 1997). EIT is a medical imaging modality that can be used to reconstruct an *in vivo* conductivity map by generating a current distribution inside a conductor and measuring the surface voltage profile. The technique can be classified as injected-EIT (Rigaud and Morucci 1996) if the probing current is applied to the volume conductor via surface electrodes and as induced-EIT (Freeston and Tozer 1995, Gençer *et al* 1997) if coils placed around the object are used for current generation. For both approaches, the sensitivity of peripheral voltage measurements to conductivity perturbations is position dependent and poor for inner regions. Consequently, the reconstructed conductivity image has a space-dependent resolution. In addition, the sensitivity and resolution degrade as the distance to the surface increases (Köksal and Eyüboğlu 1995, Eyüboğlu *et al* 2000a, Köksal *et al* 2002). The best practical resolution is limited to 10% of the electrode array diameter (field of view) (Eyüboğlu *et al* 1989).

Another approach for conductivity reconstruction is the use of a magnetic field measured using magnetometers (Ahlfors and Ilmoniemi 1992). In this technique, the current is generated using surface electrodes and the resulting magnetic field is measured outside the object. In a similar technique, called magnetic induction tomography (Korjenevsky *et al* 2000), coils placed around the object are used for both current induction and magnetic field measurement. In both these approaches, the problem of lower sensitivity to the inner regions still exists.

An alternative method for conductivity reconstruction is based on measuring the magnetic flux density generated by the applied currents using magnetic resonance imaging (MRI) techniques (Zhang 1992). Using MRI, the magnetic flux density in the inner parts of the volume conductor can be measured (Maudsley *et al* 1984). It has been shown that the magnetic flux density due to injected dc (Scott *et al* 1991, 1992, Eyüboğlu *et al* 1988, Özbek *et al* 2001, Özbek 2002), radio frequency (RF) (Scott *et al* 1995) and ac (İder and Müftüler 1995, 1997, Mikac *et al* 2001) currents can be measured using MRI techniques. Reconstruction of current density distribution based on magnetic flux density measurement is possible and the technique is called magnetic resonance-current density imaging (MR-CDI). Zhang (1992) proposed an image reconstruction algorithm using internal current density and peripheral voltage measurement to reconstruct static conductivity images. Zhang's algorithm is based on the fact that a potential difference measured on the surface between two points can be expressed as $\int_C (1/\sigma) \vec{J} \cdot d\vec{l}$, where σ is the tissue conductivity, \vec{J} is the current density and C is any arbitrary path connecting the measurement points. Woo *et al* (1994) also suggested the use of internal current density distribution and peripheral voltage for impedance imaging and presented simulation results for a sensitivity-based reconstruction algorithm. Conductivity images, reconstructed using only experimental magnetic flux density data, for cases of ac and dc current are presented in the works of İder and Birgül (1998) and Birgül *et al* (2001a), respectively. The disadvantage of this approach is that the reconstructed conductivities are not the true values. Birgül *et al* proposed a double-constraint reconstruction algorithm that combines magnetic flux density measurements of MRI with voltage measurements of conventional EIT technique to find the true conductivity values (Birgül *et al* 1999, 2001b, Eyüboğlu *et al* 2000b, 2001). Using the same idea, Kwon *et al* (2002a) developed an alternative true conductivity reconstruction algorithm called the J -substitution algorithm and tested the algorithm using simulated data. They claim that if at least two current injection patterns satisfying $|\mathbf{J}^1 \times \mathbf{J}^2| \neq 0$ are used together with a single voltage measurement, true conductivity can be reconstructed. Khang *et al* (2002) attempted to reconstruct the image of an insulator object using the same algorithm. Eyüboğlu *et al* (2002) and Özdemir and Eyüboğlu

(2002) suggested a linear reconstruction algorithm based on constructing equipotential lines in the imaging region using peripheral voltages and current density distribution. The current density inside the object is measured and it is known that the equipotential lines and current lines are orthogonal. The potential, thus the electrical field, distribution inside the object can be found by finding the equipotential lines and projecting the peripheral voltage measurements into the field of view (FOV) along these lines. Using the calculated electric field distribution and measured current density distribution, conductivity can be found for the entire FOV. Kwon *et al* (2002b) also implemented the equipotential line method.

The ability of an EIT system to distinguish an inhomogeneity in a conductive medium is referred to as ‘distinguishability’ in the EIT literature (Isaacson 1986). Several distinguishability measures have been developed for the conventional EIT technique (Isaacson 1986, Gisser *et al* 1988, Cheney and Isaacson 1992, Eyüboğlu and Pilkington 1993, Köksal and Eyüboğlu 1995). Isaacson (1986) showed analytically that cosine current injection provides better distinguishability than opposite current injection if the peak of the cosine is set equal to the current in the opposite injection. Considering that the power that can be supplied from an instrument is limited, the peak value of the cosine current can be adjusted to maintain the same power applied in the case of the opposite current injection (Cheney and Isaacson 1992) and for the same power situation, the cosine injection still shows better performance than for the opposite current case. In a later study, Eyüboğlu and Pilkington (1993) stated that, to satisfy the existing medical device safety regulations, not the peak value of the current or total power but the total current applied to the subject should be kept the same. In order to choose an optimum current injection strategy, the performance of the algorithm proposed in this paper is studied for opposite and cosine probing current patterns.

In this study, a current density constrained voltage scaled (CCVSR) MR-EIT reconstruction algorithm for true conductivity imaging is presented. Both the peripheral voltage measurements and the magnetic flux density measurements due to injected currents are used for image reconstruction. It differs from the double-constraint algorithm proposed by the same group (Birgül *et al* 2001b) in the usage of the peripheral voltage measurements. In Birgül *et al* (2001b), the electric field inside the object is found by solving the related boundary value problem by imposing the potential measurements as Dirichlet boundary conditions first. Then, the calculated field is used together with the current density measurements of MRI to find the conductivity distribution. In this method, the solution at the boundary contains high error and causes divergence of the algorithm in the presence of noise. In the CCVSR algorithm, magnetic flux density measurements are used to find a fine detailed conductivity image first and then the image is scaled to satisfy the voltage measurements. Kwon *et al* (2002a) also used the idea of scaling in their algorithm. The difference between the CCVSR algorithm and Kwon *et al*'s (2002a) J -substitution algorithm is in the selection of current injection strategy and combination of the measurements for different current injections. They apply two current patterns in two different orientations. In each iteration, the image is updated twice. First, using data from one current injection, a new image is formed. Then, the new image is used in the forward problem for the second current injection case and the image is updated again using the data from the second current injection. However, in this study we used eight rotations of current injection and used the measurements simultaneously to constrain the reconstruction. Another difference between the two studies is in the addition of noise in simulations. We add noise to the magnetic flux density distribution and calculate the current density from this noise-added magnetic flux density, whereas Kwon *et al* (2002a) add simulation noise directly to the current density values. Adding noise to the magnetic flux density is a more realistic approach.

In the following sections, the proposed measurement methods for peripheral voltages and magnetic flux density distribution are explained and an iterative conductivity update algorithm

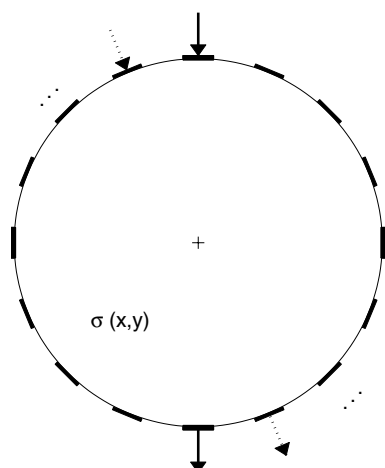


Figure 1. Electrode positions and coordinate definitions for the 2D problem. The radius of the imaging region is set to 12 cm.

is derived. The forward solvers used in the reconstruction algorithm and in the generation of simulated peripheral voltage measurements and magnetic flux density are explained in section 3 together with expressions used to determine the reconstruction error. After presenting the studies on selection of current injection strategy, the results of accuracy and the spatial and contrast resolution studies based on this selection are discussed. Finally, images reconstructed for a complex conductivity distribution, which is designed to model the human thorax, are presented.

2. Reconstruction of conductivity

The inverse problem, or image reconstruction, is the calculation of conductivity distribution inside an object using measured peripheral voltage and inner magnetic flux density distributions. Peripheral voltages and magnetic flux density can be measured using conventional EIT techniques and MRI techniques, respectively. If the applied current is kept the same, two conductivity distributions, σ and $\kappa\sigma$, where κ is a positive scaling factor, generate the same internal current density and magnetic flux density distributions. Thus, the true conductivity value cannot be reconstructed when magnetic flux density alone is used. Our aim is to find a conductivity image σ using magnetic flux density measurements and then calculate the scaling factor κ using voltage measurements to find the true conductivity values. The same approach is also used in Kwon *et al* (2002a). In this section, first the measurement strategies are described, and then the reconstruction algorithm is explained.

2.1. Current injection and voltage measurement strategy

For the two-dimensional problem given in figure 1, 16 electrodes are placed around the object. For the opposite-drive (OPP) strategy, two electrodes that are 180° apart are used as current injection and sink electrodes, and the voltages at the remaining 14 electrodes are measured with respect to a reference electrode at a distant point. As a result, a total of 112 measurements can be made using eight different drive pairs of the electrodes. In practical realization of the technique, large metal electrodes may cause susceptibility artefacts which may destroy the

MR signal originating from the regions close to the electrodes. However, using thin metal electrodes or conducting rubber electrodes, this problem can be substantially reduced based on our preliminary experimental observations.

Three different constraints are used for the cosine current injection case. For the same maximum (SM) current case, the peak current in the cosine current injection scheme is selected to be equal to the current injected in the opposite drive case. For this case, the total power applied to the object is 8.93 times the power applied for the opposite current drive. For the same power (SP) case, the current is scaled to have equal powers for the opposite and cosine current injections. The peak current in SP cosine injection is 34% of the current applied in the opposite current case. The last case is the same total (ST) current case where the total current applied during cosine injection is set equal to the opposite drive current value. For this case the peak cosine current is 20% of the opposite current and the power is 33% of the power applied during opposite current injection. For the SM and SP cases the total current applied is 500% and 170% that of the current applied in the opposite current case, respectively. The percentages given above are calculated for the thorax model given in figure 4.

2.2. Magnetic flux density measurements

The magnetic flux density generated by the current flow in the volume conductor can be obtained using MRI techniques, for each of the eight current injection profiles. The magnetic flux density cannot be measured directly but is extracted from MR phase images acquired during current injection.

The magnetic flux due to the current applied during MR data acquisition accumulates an additional phase in the resulting MR image. Although the current induced magnetic flux, \vec{B}_J , has components in three directions, only the component which is parallel to the main magnetic field, $B_{J,z}$, causes phase accumulation. In order to measure this phase, the MR pulse sequence in Scott *et al's* (1991) work can be used. This is a conventional spin echo pulse sequence with an additional bipolar current pulse, applied synchronously with the sequence. A detailed discussion of the MR-CDI pulse sequence that can be used to measure the current induced phase, and the images of the corresponding magnetic field distributions acquired using a similar MR-CDI pulse sequence are presented elsewhere (Scott *et al* 1991, 1992, Eyüboğlu *et al* 1988). This type of current density imaging is referred to as dc current density imaging; however, the current pulse is bipolar and the switching frequency is around 20–30 Hz. At this frequency, IEC601 specifies a safety limit of 100 μA for *patient auxiliary current*. The image reconstruction algorithm proposed in this study can be applied to measurements made at any frequency. Therefore, the technique is applicable to MR-CDI measurements obtained by using dc (Scott *et al* 1991, 1992, Eyüboğlu *et al* 1988, Özbek *et al* 2001), radio-frequency (RF) currents (Scott 1995 *et al*) or AC currents at frequencies up to 2 kHz (İder and Müftüler 1995, 1997, Mikac *et al* 2001). With improved MRI systems capable of applying hard RF pulses with higher amplitude and shorter duration, imaging of ac currents higher than 2 kHz may be possible (Mikac *et al* 2001). As the frequency of injected current increases, the IEC601 safe current limit increases. At 10 kHz, the IEC601 safety limit for the *patient auxiliary current* is equal to 1 mA.

In an MRI experiment, the phase of the complex MR image is wrapped between 0 and 2π . However, the phase induced due to the injected current can be more than 2π in general. Although this situation does not occur in the simulation data used in this study, in the case of real data, in order to obtain the correct magnetic field distribution, a phase unwrapping algorithm must be applied to the phase images. Liang's model based phase unwrapping can be used for this purpose (1996). This algorithm fits a polynomial to the derivative of the

measured phase and adds a residual function to the integral of the fitted polynomial which guarantees that no noise is introduced during unwrapping (Liang 1996).

2.3. Image reconstruction algorithm

The image reconstruction or the solution of the inverse problem involves calculation of the conductivity distribution using the measured peripheral voltage values and the measured inner magnetic flux density distribution. In this study, an iterative reconstruction algorithm based on Ohm's relation is utilized. Before iterations are started, current density distribution is calculated from the magnetic flux density distribution. The relation between current density and magnetic flux density is given by

$$\vec{J}_{MR} = \frac{\nabla \times \vec{B}_{MR}}{\mu_0} \quad (1)$$

where \vec{B}_{MR} is the magnetic flux density extracted from MR measurements. Note that \vec{J}_{MR} is calculated once and remains unchanged during the iterations. Given the measurements of the current density \vec{J}_{MR} for all points in S , where S is the imaging region, i.e. the object, and the measurements of the peripheral voltages ϕ_m , our aim is to determine the true conductivity distribution σ_f .

The steps of one iteration are as follows:

- (i) An initial conductivity distribution, σ_{ini} , is assumed. This initial conductivity distribution is selected to be uniform for the first iteration.
- (ii) The peripheral voltage values, ϕ_{ini} , corresponding to σ_{ini} , are calculated, by solving (4) and (5) below.
- (iii) The scaling factor, k , is found such that the function

$$F = \left\| \frac{1}{k} \phi_{ini} - \phi_m \right\| \quad (2)$$

is minimized with respect to k .

- (iv) The conductivity is scaled using k as

$$\sigma_s = k \sigma_{ini} \quad (3)$$

where σ_s represents the scaled conductivity.

- (v) The electric field distribution, \vec{E} , inside the object for the conductivity distribution, σ_s , is calculated solving the boundary value problem (BVP) given by the following equation and the Neumann boundary conditions:

$$\nabla \cdot (\sigma_s \nabla \phi) = 0 \quad \text{in } S \quad (4)$$

$$-\sigma_s \frac{\partial \phi}{\partial n} = \begin{cases} J_{app} & \text{on positive current electrodes} \\ -J_{app} & \text{on negative current electrodes} \\ 0 & \text{elsewhere} \end{cases} \quad (5)$$

where σ_s is the (scaled) conductivity distribution, ϕ is the electric potential distribution, $\frac{\partial \phi}{\partial n}$ is the derivative of the electrical potential in the direction of the outward normal and J_{app} is the magnitude of applied current density. Once the potential distribution inside the object is found by solving the above boundary value problem (BVP), the electric field is found by using

$$\vec{E} = -\nabla \phi. \quad (6)$$

A residual function is defined as

$$R = \sum_j \int_S \|\sigma_r \vec{E}_j - \vec{J}_{MR,j}\|^2 ds \quad (7)$$

where j (i.e. $j = 1$ to 8) is the current injection profile index (Wexler *et al* 1985), and σ_r is the reconstructed conductivity. Note that minimizing this residual function imposes the satisfaction of Ohm's law in the object for all current injection patterns simultaneously. S can be divided into non-overlapping elements S_i such that $\bigcup S_i = S$ and the conductivity in each element is assumed to be uniform. Minimizing the residual function with respect to the conductivity of each element, the update equation for that pixel's reconstructed conductivity is obtained as

$$\sigma_{r,i} = \frac{\sum_j \int_{S_i} \vec{E}_j \cdot \vec{J}_{MR,j} ds}{\sum_j \int_{S_i} \vec{E}_j \cdot \vec{E}_j ds} \quad (8)$$

where $\sigma_{r,i}$ is the i th pixel's reconstructed conductivity.

- (vi) If the stopping criterion explained in the next section is met, then the iterations are terminated. Otherwise, σ_{ini} is replaced with σ_r and the steps are repeated until a stopping criterion is met.

In equation (8), the data for different current injection cases are used simultaneously to improve the quality of the reconstructed image. We used eight different current injection patterns in the simulations. In Kwon *et al*'s (2002a) work, two sets of measurements are used separately and the conductivity distribution is updated twice in each iteration. As the algorithm converges, \vec{J} and \vec{E} will have the same direction and for a single current injection case, the ratio

$$\frac{\vec{E} \cdot \vec{J}}{\vec{E} \cdot \vec{E}} \quad (9)$$

used in the algorithm will approach the ratio

$$\frac{\|\vec{J}\|}{\|\vec{E}\|} \quad (10)$$

which is used in Kwon *et al*'s (2002a) algorithm. Both can be used as long as convergence is attained.

2.4. Error calculation and stopping criteria

In order to evaluate the performance of the proposed algorithm, two error expressions are defined. The potential error is defined, based on measured peripheral voltages, ϕ_m , and surface potential values at electrodes calculated using the reconstructed conductivity distribution, ϕ_c , as

$$\varepsilon_\phi = \sum_j \frac{\|\phi_{m,j} - \phi_{c,j}\|}{\|\phi_{m,j}\|} \times 100\% \quad (11)$$

where j is the current injection profile index.

The second error expression is defined to test the performance of the algorithm in simulation studies. The conductivity error requires knowledge of the real conductivity distribution, and therefore cannot be calculated in general. However, it is useful in

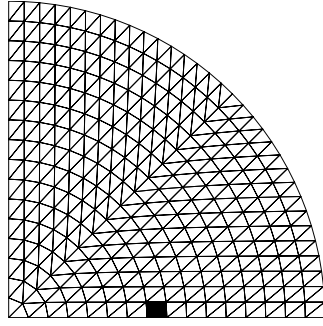


Figure 2. First quadrant of the symmetric FE mesh used. The total numbers of elements and nodes are 2048 and 1089, respectively. The shaded region is a typical point object.

understanding the relation between the potential error and the corresponding conductivity error in simulation studies. Using the true and reconstructed conductivity values, the conductivity error is defined as

$$\varepsilon_{\sigma} = \sqrt{\frac{1}{N} \sum_{i=1}^N \frac{(\sigma_{t,i} - \sigma_{r,i})^2}{\sigma_{t,i}^2}} \times 100\% \quad (12)$$

where $\sigma_{t,i}$ and $\sigma_{r,i}$ are the true and reconstructed conductivity values for the i th pixel, and N is the total number of pixels in S .

In order to terminate the iterative reconstruction algorithm, error expression (11) is used. The stopping criterion is based on the observations made during the numerical experiments. As the iterations proceed, ε_{ϕ} either decreases monotonically or in the case of noisy data, it reaches a minimum and starts increasing afterwards. In the case of a monotonically decreasing behaviour, 20 iterations are performed. However, in the case of divergent behaviour, the iteration corresponding to the minimum ε_{ϕ} is taken as the terminal iteration.

3. Simulation of potential and current density measurements

In this study, simulations are made for conductive objects in the form of thin discs of 12 cm radius and 1 mm thickness. The direction along the thickness is taken as the z direction and z ranges between 0 and 1 mm. We further assume that σ does not vary in the z direction and that the electrodes are 1 mm thick as well. In such a geometry the current density inside the object is z independent. Therefore, \vec{J}_{MR} is a two-dimensional current density with J_x and J_y components only.

3.1. Finite element model used for electric field and current density solutions

The analytical expression for the solution of the BVP in (4) and (5) does not exist in general. In order to calculate the electric field distribution for our simulations, the finite element method (FEM) is employed. Since all system variables are z independent, a two-dimensional FEM formulation can be used. To generate simulation data for a known conductivity distribution, ϕ_m and \vec{J}_{MR} are also calculated using the same model. The FEM mesh given in figure 2 has 1089 nodes and 2048 first-order triangular elements. The electric potential is assumed to vary linearly inside an element and, therefore, the current density in each element is constant. Each current injection electrode is assumed to cover two finite element edges. The shaded region

in figure 2 demonstrates a typical point object, comprising two elements, used in simulation studies.

3.2. Simulation of measurement noise

The electrode voltage, ϕ_m , and internal current density distribution, \vec{J}_{MR} , measurements are required by the proposed reconstruction algorithm. In order to understand the behaviour of the algorithm in the presence of noise, simulated noisy potential and current density data are used.

To decide on the level of noise to be added to the voltage measurements, typical noise levels reported for conventional EIT hardware previously are considered. In Eyüboğlu (1988), the maximum value of the noise for adjacent current injection is reported as 1% of the minimum measurement. In our study, we used uniformly distributed noise for voltage measurements. The maximum value of voltage noise is taken as 3% of the maximum voltage measurement in the opposite current injection strategy. For these noise levels, the maximum value of the noise is larger than the minimum measurement for the simulation objects used in this study.

In actual experiments, \vec{J}_{MR} values are in fact calculated from \vec{B}_{MR} measurements. Therefore, noise should be added to \vec{B}_{MR} . In order to generate simulation noise to be added to magnetic flux density measurements, the random noise definition explained by Scott *et al* (1992) is used. In their work, the signal-to-noise ratio (SNR_{MR}) is defined as

$$\text{SNR}_{MR} = \frac{A}{s_n} = \Psi_s \Delta x \Delta y \Delta z \sqrt{N \cdot T_s} M(x, y) \quad (13)$$

where A is the magnitude of the noise-free pixel value of the corresponding MR image, s_n is the complex image noise standard deviation and is measured as the rms noise in the magnitude image background, Ψ_s is a system SNR, $\Delta x \Delta y \Delta z$ is the voxel volume, N is the total number of excitations (averages times phase encodes), T_s is the readout sampling time for one echo, and $M(x, y)$ is magnetization. The phase error probability density function is given by

$$f_{\Theta}(\theta) = \frac{1}{2\pi} \exp(-a^2/2) + \frac{a \cos(\theta)}{2\sqrt{2\pi}} \exp(-a^2) \sin^2(\theta)/2 \operatorname{erfc}(-a \cos(\theta)\sqrt{2}) \quad (14)$$

where $a = \sqrt{2}\text{SNR}_{MR}$ and, θ represents phase error. Scott *et al* (1992) reported an SNR_{MR} measurement of 30 with a 2 T magnet. We have found that for our 0.15 T METU MRI system, the SNR_{MR} value is around 13 with similar conditions and four averages.

Note that in the noise model of Scott *et al* (1992) the phase error and hence, the noise in \vec{B}_{MR} , is independent of \vec{B}_{MR} . Therefore, for increased amount of current density, since \vec{B}_{MR} is also increased, the proportional noise in \vec{B}_{MR} is reduced. Similarly, in such a case the proportional noise in \vec{J}_{MR} is also reduced. Using this noise model allows us to compare various current injection strategies under the same noise condition. Furthermore, as opposed to, for example, adding uniformly distributed noise to \vec{J}_{MR} proportional to its magnitude, the noise model of Scott *et al* (1992) provides a means for incorporating a more realistic and experimentally verified noise probability density function into the simulations.

In order to understand the performance under different noise levels, we carried out simulation studies for SNR_{MR} equal to 30, 20 or 10. For the opposite-drive current injection strategy, SNR_{MR} levels of 30, 20 and 10 results in maximum noise levels in J_x and J_y of approximately 4%, 7.5% and 13.5% of the maximum current density, respectively. Standard deviations of the noise for SNR_{MR} levels of 30, 20 and 10 are approximately 1%, 1.5% and 2.9% of the maximum current density, respectively. These noise levels are comparable, in high current regions, to the 5% and 2.5% proportional noise added to J_x and J_y in Kwon *et al*

(2002a). However, the noise ratios used in our study significantly underestimate the amount of noise in the inner regions where the current density is smaller.

For the purpose of obtaining noisy \vec{J}_{MR} we utilized the following procedure: for a given \vec{J}_{MR} distribution \vec{B}_{MR} is calculated at a plane 5 mm above the centre plane of the disc. For this purpose we have assumed that for each finite element the current is localized at the centre of that element and at mid-plane of the disc ($z = 0.5$ mm). The relation between magnetic flux density and current density is approximated as a matrix equation by discretizing the Biot–Savart law

$$\vec{B} = \frac{\mu_0}{4\pi} \int \frac{\vec{J} dS \times \hat{a}_R}{R^2} \quad (15)$$

where R is the distance between the source and a field point and \hat{a}_R is the unit vector from the source point to the field point, to obtain

$$\begin{bmatrix} \mathbf{b}_x \\ \mathbf{b}_y \\ \mathbf{b}_z \end{bmatrix} = \begin{bmatrix} \mathbf{0} & \mathbf{D}_z \\ -\mathbf{D}_z & \mathbf{0} \\ \mathbf{D}_y & -\mathbf{D}_x \end{bmatrix} \begin{bmatrix} \mathbf{j}_x \\ \mathbf{j}_y \end{bmatrix} \quad (16)$$

where $\mathbf{j}_x, \mathbf{j}_y$, are the column vectors of J_x, J_y values for the finite elements, respectively, and $\mathbf{b}_x, \mathbf{b}_y, \mathbf{b}_z$ are the column vectors of B_x, B_y, B_z values at the field points, respectively. The elements of the matrices $\mathbf{D}_x, \mathbf{D}_y$ and \mathbf{D}_z depend on the magnitude and the direction of the \vec{R} vectors between the field and source points. Since these matrices are constant for a mesh structure, they can be calculated once and stored.

For a given simulated \vec{J}_{MR} obtained by the FEM solution, we calculated \mathbf{b}_x and \mathbf{b}_y on a mesh 5 mm above the mid-plane of the thin disc. This mesh is the same as that shown in figure 2 and the field points are taken as the element centres. Then noise is added to this calculated \mathbf{b}_x and \mathbf{b}_y , and noisy \mathbf{j}_x and \mathbf{j}_y values are calculated by using the inverse of the \mathbf{D}_z matrix. This matrix is a well-conditioned one with a condition number of 35. Therefore, the transformation from \vec{B}_{MR} to \vec{J}_{MR} introduces an insignificant error in \vec{J}_{MR} when no noise is added to \vec{B}_{MR} .

We verified that \vec{B}_{MR} calculated as described above contains 0.77% maximum error in B_x and 0.32% maximum error in B_y compared to those calculated using a three-dimensional FEM mesh with ten layers within a 1 mm thick disc with uniform conductivity. Since B_x values are smaller, the maximum per cent error in B_x is larger as expected.

In the simulations voltage noise is always taken as 3% as explained above, and the value of SNR_{MR} is specified to denote the amount of noise in \vec{J}_{MR} data. Examples of B_x and B_y obtained for a homogeneous conductivity with no noise and with $\text{SNR}_{MR} = 20$ noise for OPP strategy, and the corresponding current density magnitude images are given in figure 3. In order to use the greyscale dynamic range optimally, the regions close to the electrodes (1.5 cm from the surface of the 12 cm radius disc), which have high current density, are masked in these images. These images give an idea about the significance of the noise added to \vec{J}_{MR} , using the noise model of Scott *et al* (1992), especially in the low \vec{J}_{MR} regions.

4. Results

4.1. Selection of current injection strategy

The optimum current injection strategy changes with the conductivity distribution, and it is not easy and practical to determine the optimum current for every conductivity distribution. In order to decide on the current injection strategy, the opposite and cosine current patterns are

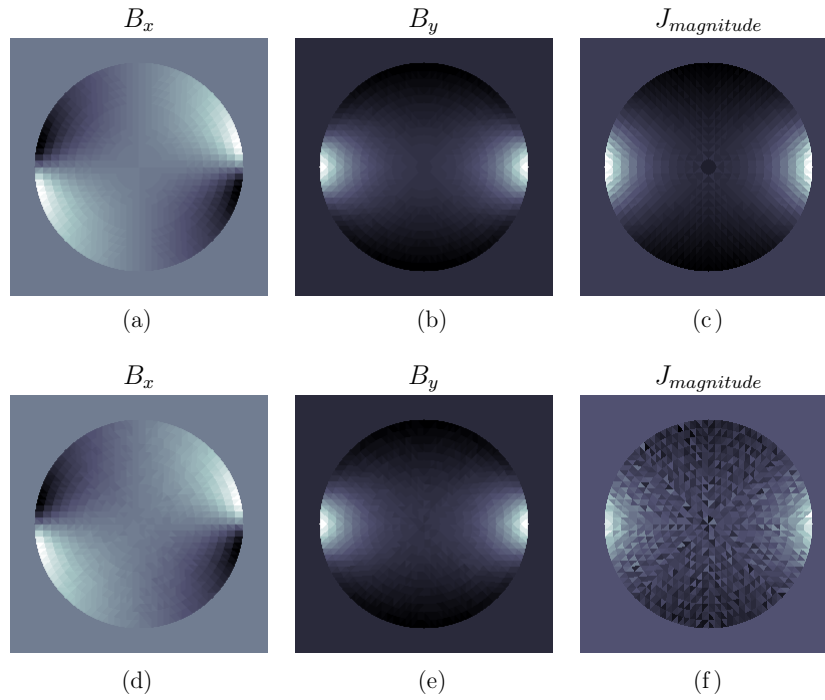


Figure 3. B_x , B_y and the corresponding current density magnitude images with no noise and with $\text{SNR}_{\text{MR}} = 20$ noise, for the OPP strategy when the current is applied between the leftmost and the rightmost electrodes on the surface of a disc with uniform conductivity distribution. (a), (b) and (c) are the noise-free B_x , B_y and current density magnitude images; (d), (e) and (f) are the corresponding noisy images.

Table 1. Thorax model values (S cm^{-1}).

Region	Tissue	Assigned value
1	Blood	6.67×10^{-3}
2	Myocardium	1.54×10^{-3}
3	Lung	7.69×10^{-4}
4	Bone	6.02×10^{-5}
5	Background	2.00×10^{-3}

studied, and by examining the errors in reconstructed images, the performance of each current pattern is compared for a thorax model.

The model in figure 4 is designed to simulate the human thorax to evaluate the performance of the algorithm with different current injection patterns. The assigned conductivity values of different tissues are listed in table 1. The conductivity and the potential errors for noise-free and noisy cases and for different current injection patterns are given in figures 5(a)–(d). When the error plots are compared it is seen that under noise-free cases, all current injection strategies have similar convergence behaviour. However, in the presence of noise, SM shows the best performance. Although the opposite current injection case is inferior to the SM and SP cases, the error values for the opposite current case are less than the errors for the ST case. The original thorax model and the reconstructed conductivity images using data with

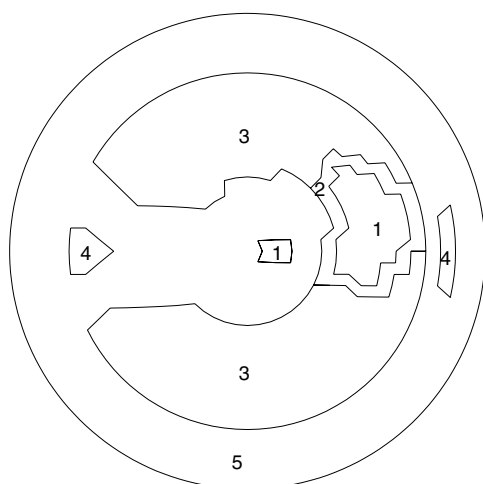


Figure 4. Definitions for the thorax model. The conductivity values for different regions are given in table 1.

Table 2. Results of spatial resolution study.

	ε_ϕ (%)	ε_σ (%)
Noise free	<1	<1
SNR _{MR} = 30	4.19	3.18
SNR _{MR} = 20	4.53	4.69
SNR _{MR} = 10	5.01	9.74

SNR_{MR} equal to 20 for different current injection strategies are presented in figure 6. The best image is obtained for the SM case, in parallel with the reconstruction error plots. The opposite current case is worse than the SM and SP cases but better than the ST case. Using the results presented in figures 5 and 6 and considering the existing safety regulations, we decided to use opposite current injection for our studies. Although SM and SP give better results, safety problems may arise due to the higher total current. Several studies are carried out to further understand the performance of the algorithm for the opposite current injection and the results are presented in the next section.

4.2. Spatial resolution and contrast studies

The sensitivity of the reconstruction algorithm to regional conductivity perturbations is tested using point objects at different radial locations. A typical point object has been shown in figure 2. The background and object conductivity values are selected as 2 mS cm⁻¹ and 20 mS cm⁻¹, respectively. The iterations are stopped either when the potential error reaches a minimum or when a maximum iteration limit is reached, which is set to 20. For the noise-free case, both the potential and conductivity error values are below 1% for all locations. The potential and conductivity errors are independent of the position for both the noise-free and the noisy cases except for the case where the point object is placed just near the boundary. The results are summarized in table 2.

The full-width at half-maximum (FWHM) values are calculated for reconstructed point objects at different locations. The profile of the reconstructed image for a point object placed midway between the centre and the periphery for SNR_{MR} = 30 and SNR_{MR} = 10 noise cases

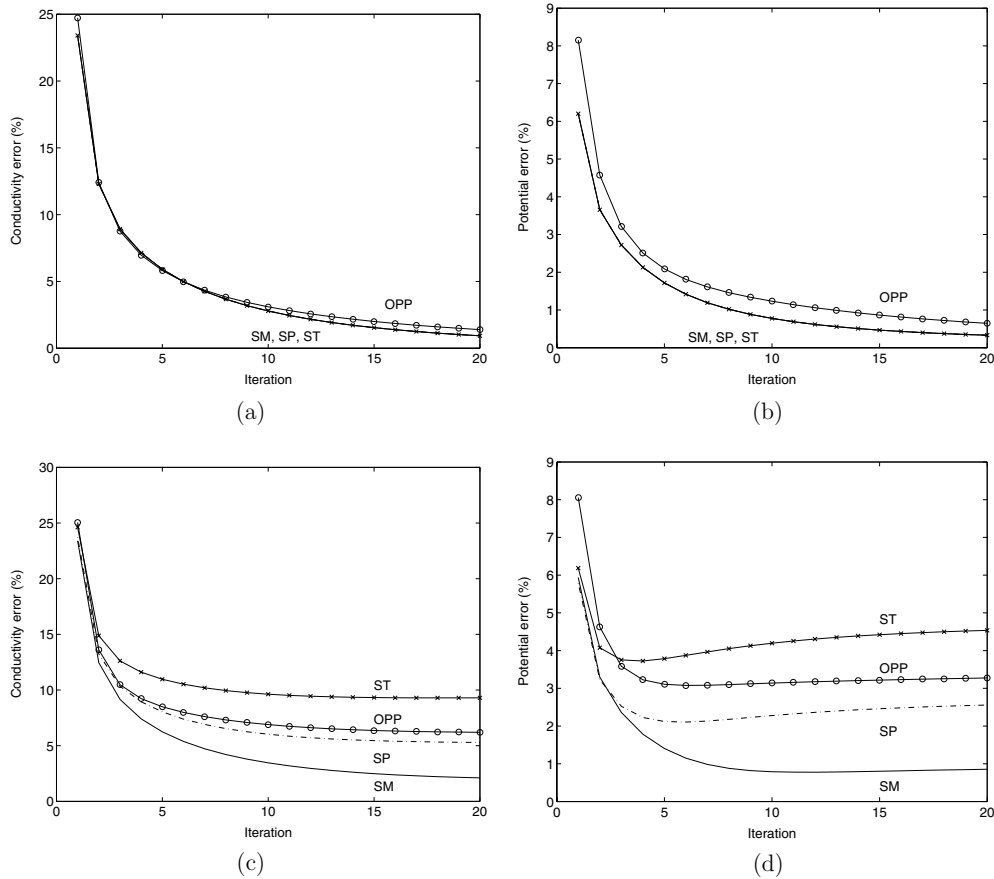


Figure 5. Conductivity and potential error plots with respect to iteration for current injection strategies for noise-free and $\text{SNR}_{\text{MR}} = 20$ cases. (a) Noise-free conductivity error, (b) noise-free potential error, (c) conductivity error in the presence of $\text{SNR}_{\text{MR}} = 20$ noise and (d) potential error in the presence of $\text{SNR}_{\text{MR}} = 20$ noise.

are given in figure 7. The FWHM values are found to be the same for all cases and equal to the size of an FE model pixel. This corresponds to 3.125% of the electrode array diameter. Therefore, for this case the resolution is limited by the FE mesh size. Another limitation on the spatial resolution is the resolution of \vec{J}_{MR} distribution which is related to the resolution of \vec{B}_{MR} via a curl operation as stated in (1). The MRI resolution determines the resolution of \vec{B}_{MR} and due to curl operation, the resolution becomes equal to half of the MR resolution. In general, the *larger element size of the FE mesh* and *twice the MR image pixel size* will determine the spatial resolution.

The limit of contrast resolution is determined by examining the standard deviation of conductivity in reconstructed images for a uniform conductivity distribution for different noise levels. The conductivity value is selected as the average human conductivity, 2 mS cm^{-1} . The standard deviation values in reconstructed conductivity are found to be 0.08 mS cm^{-1} , 0.12 mS cm^{-1} and 0.25 mS cm^{-1} for $\text{SNR}_{\text{MR}} = 30, 20$ and 10 noise cases, respectively. As normalized to 2 mS cm^{-1} , the contrast resolution becomes 4%, 6% and 12.5% for 30, 20 and 10 noise cases, respectively.

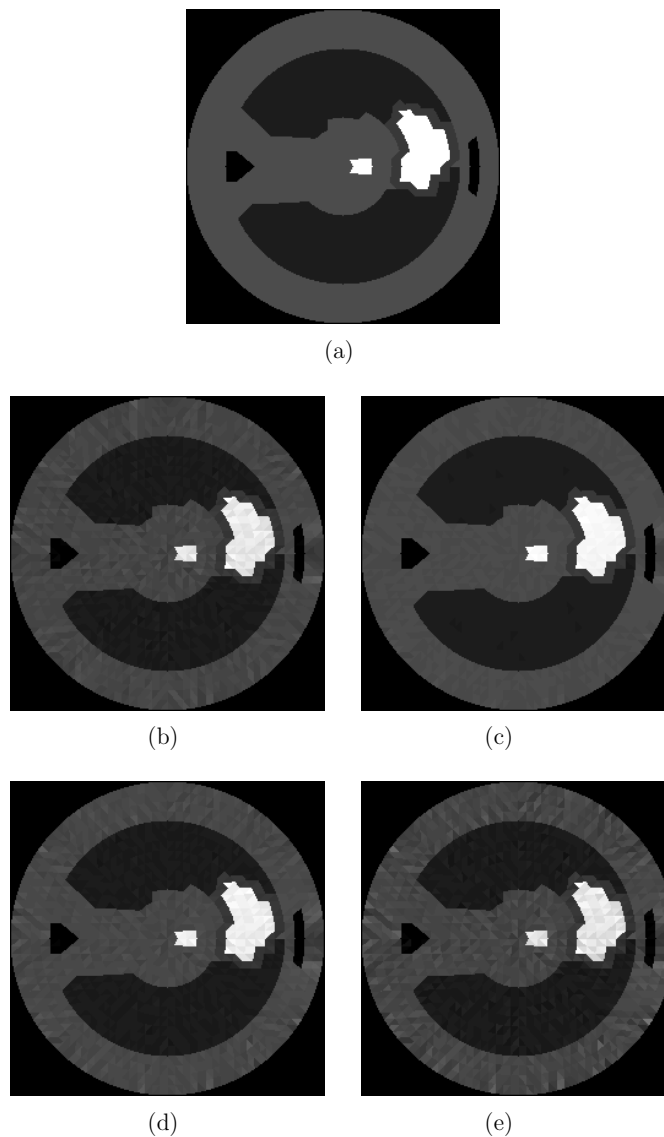


Figure 6. (a) Original distribution. The other frames are reconstructed thorax images for different current injection strategies with $\text{SNR}_{\text{MR}} = 20$ noise case for (b) opposite current, (c) cosine, same maximum current, (d) cosine, same total power and (e) cosine, same total current.

4.3. Accuracy of the reconstructed conductivity values

The accuracy of the reconstructed conductivity values is tested by carrying out a set of simulation studies for which the conductivity of a circular object with a radius of 3 cm at the centre of the imaging plane is varied between 0.01 mS cm^{-1} (highly insulating) and 100 mS cm^{-1} (highly conducting). Images are reconstructed for 12 different conductivity levels which are equally spaced in logarithmic scale between the two extreme values. The average reconstructed conductivity in the circular object region is calculated for all cases and plotted against the actual conductivity value. The study is carried out for different noise levels

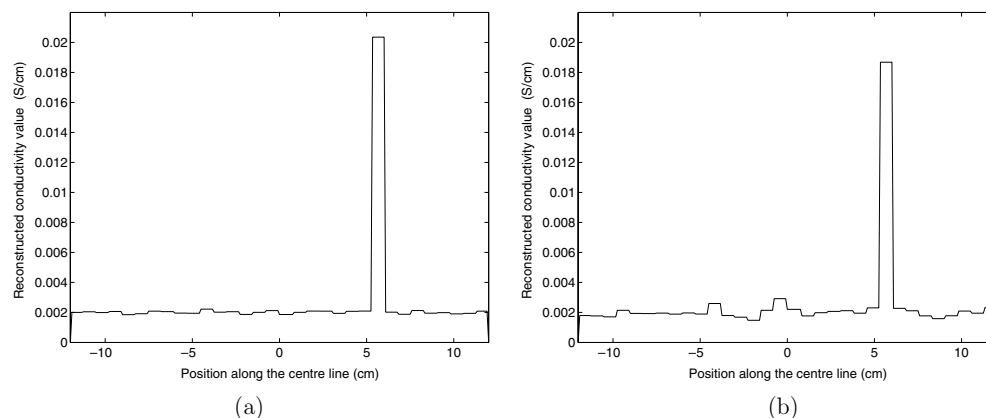


Figure 7. Profile of the image along the centre line reconstructed for a point object: (a) $SNR_{MR} = 30$ noise, (b) $SNR_{MR} = 10$ noise.

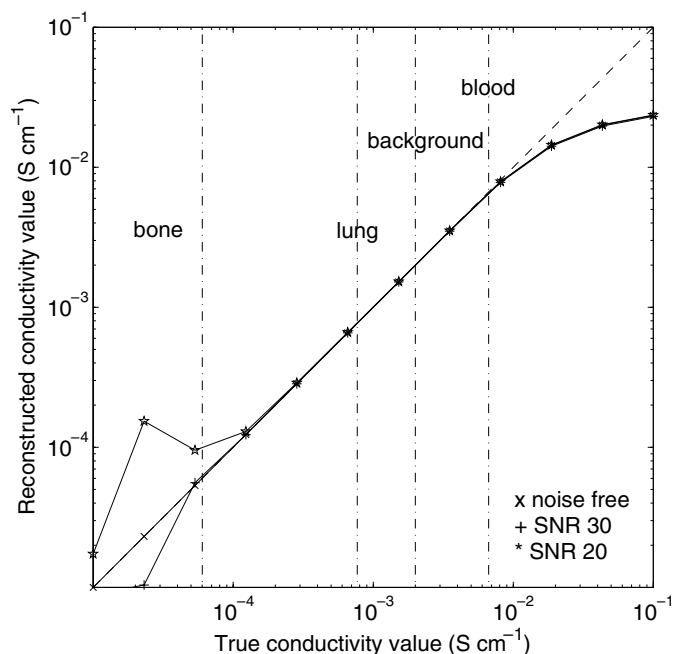


Figure 8. Accuracy of the reconstructed conductivity.

and the results are presented in figure 8. The dashed line with unity slope corresponds to the ideal reconstruction where the actual and reconstructed conductivity values are the same. Both axes are drawn in logarithmic scale. The dash-dotted vertical lines are the conductivity values of various tissues in the human body. The conductivity values for some tissues in the human body are given in table 1. The background conductivity is the average human conductivity. For the noise-free and $SNR_{MR} = 30$ cases, in the bone-to-blood conductivity range, the conductivity of the 3 cm object is found almost exactly. In the $SNR_{MR} = 20$ case, for the bone conductivity and lower values, the errors in the average conductivity of the reconstructed object are large. Since current density in a highly resistive bone object

is expected to be very low, with the addition of noise, such high inaccuracies are expected. In conclusion, the conductivity of most tissues lies in a region where it can be estimated accurately.

5. Discussion and conclusion

The numerical experiments in this paper show that the proposed MR-EIT method has the capability of reconstructing high resolution true conductivity images. The classical injected EIT technique makes use of peripheral voltage measurements only. However, the proposed technique utilizes both the peripheral voltage measurements and the magnetic flux density measurements extracted from MRI phase images. Peripheral voltage measurements have low sensitivity to inner region perturbations. On the other hand, the sensitivity of the magnetic flux density measurements to regional conductivity perturbations is position independent. The method proposed in this study uses magnetic flux density measurements to reconstruct the fine detail of the inner conductivity distribution with uniform resolution throughout the object except for a scale factor. The peripheral voltage measurements are only used to scale the reconstructed conductivity distribution in order to obtain true values. Therefore, this technique is superior to conventional EIT techniques in which the resolution for inner regions is considerably low (Eyüboğlu *et al* 1989).

Current injection strategy may also determine the reconstructed image quality, and, therefore, the proposed algorithm is tested for different current injection strategies. In the presence of noise, in order to have equal vulnerability to noise throughout the imaging region, the current density inside the object must be uniform. For the opposite current injection case, the highest current density is obtained close to the electrodes. To achieve better current density uniformity inside a circular object, a cosine current injection pattern is required. When a cosine current injection pattern is used, the peak current, the total power or the total current can be specified. If the SM or SP strategy is selected, since additional current is injected using all electrode pairs, the total applied current increases, which may cause a safety problem. Therefore, considering the existing patient auxiliary current safety limits, the total current must be kept the same as in the opposite injection. By doing so, although the current density distribution has better uniformity inside the object, its value is low and large errors occur in the presence of noise. We suggest the use of opposite current injection with eight rotations. Rotating the opposite electrode pair guarantees high current density in different regions for different rotations. When we observe the error plots for different cases, the opposite current case with rotation gives a better performance than the ST case in the presence of noise.

In our simulation studies, current distribution in the object is not uniform for the opposite current case due to the fact that current is injected from a single electrode pair. The ratio of the maximum current density to the minimum is about 30 in the imaging region. Therefore the noise in low current regions is approximately 30 times the noise in the high current regions. In some noisy simulations, the iterative algorithm has a divergent behaviour. The errors made in the conductivity values in a certain iteration yield inaccurate electric field calculations for the next iteration. The update equation (8) applies Ohm's law on a pixel basis and a smoothing constraint is not imposed. Consequently, the errors in the electric field then induce further errors in conductivity. This results in a divergent behaviour as iterations proceed. Divergent behaviour is especially prominent in the peripheral regions and in such cases, we have observed that enforcing the outer 1 cm thick layer to background conductivity remedies the problem.

The resolution study is carried out considering both the spatial and the contrast resolution limits. The FWHM values for small objects placed at different radial positions are calculated and it is found that spatial resolution is space independent. It is also found that spatial

resolution is limited by the larger element size of the FE mesh and twice the MR image pixel size. For the FE mesh used here, the limit for spatial resolution is found to be equal to the pixel size and the FWHM is found to be 3.125% of the diameter of the object. In this paper, the spatial resolution studies for highly conducting small objects are presented. However, similar spatial resolution limits are observed when the studies are performed using small objects with less conductivity than the background.

The results of the accuracy study show that the relation between the true and the reconstructed conductivity values becomes nonlinear for very high or very low conductivity values. This nonlinearity was observed and reported for conventional EIT techniques earlier (İder *et al* 1995).

In the images reconstructed for the thorax model, for both noise-free and noisy cases, the boundaries of different tissues are well defined. Even the thin layer of the myocardium is visible in the reconstructed images.

The need to align the measurement axis for the magnetic flux density parallel to the main magnetic field is an inconvenience in MRCDI measurements of dc (Scott *et al* 1991, 1992, Eyüboğlu *et al* 1988, Özbek *et al* 2001) and ac (İder and Müftüler 1995, 1997, Mikac *et al* 2001) currents, when conventional MRI systems are used. This limitation may not be that severe and can be overcome if the technique is found to be clinically useful. Several proposals can be made. One approach may be rotating (e.g. approximately 15°) the patient around the x and y axes of the MRI system and measuring the flux density in the rotated positions in addition to measuring it in a position aligned with the z -axis. Here the main magnetic field of the MRI system is assumed to be in the z direction. The amount of rotation may only be about 15° because the components of the flux density along the main magnetic field direction will still be considerable (i.e. $\sin(15^\circ) = 26\%$). Three orthogonal components of the flux density can then be extracted from the measured data. Another proposal is to manufacture an MRI magnet such that the main magnetic field can be rotated by selectively exciting different coils. This may of course require considerable R&D investment and cost but in such a case the patient would not have to be rotated at all. The rotation of the main magnetic field does not need to be 90° but rotation by about 15° should be sufficient.

The results show that MR-EIT may be capable of reconstructing true conductivity images with high spatial resolution. Research is under way on extending the algorithm to 3D and for practical realization of the technique.

Acknowledgments

This work is supported by Turkish Scientific and Technical Research Council (TÜBİTAK) research grant EEEAG-198006. This work is part of the PhD study of ÖB. BME and YZ İ are the thesis co-supervisors.

References

- Ahlfors S and Ilmoniemi R 1992 Magnetic imaging of conductivity *Proc. IEEE EMBS Conf.* pp 1717–8
- Birgül Ö, Eyüboğlu B M and İder Y Z 1999 Magnetic resonance-conductivity imaging *Proc. IEEE EMBS Conf. (Atlanta, USA)* p 1127
- Birgül Ö, Özbek O, Eyüboğlu B M and İder Y Z 2001a Magnetic resonance-conductivity imaging using 0.15 tesla MRI scanner *Proc. IEEE EMBS Conf. CD-ROM*
- Birgül Ö, Eyüboğlu B M and İder Y Z 2001b New technique for high resolution absolute conductivity imaging using magnetic resonance-electrical impedance tomography (MR-EIT) *SPIE Phys. Med. Imaging* **2** 880–8
- Boone K, Barber D and Brown B 1997 Imaging with electricity: report of the European concerted action on impedance tomography *J. Med. Eng. Technol.* **21** 201–32

- Cheney M and Isaacson D 1992 Distinguishability in impedance imaging *IEEE Trans. Biomed. Eng.* **39** 852–60
- Eyüboğlu B M 1988 Development and application of electrical impedance tomography for thoracic imaging *PhD Thesis* University of Sheffield p 48
- Eyüboğlu B M, Birgül Ö and İder Y Z 2000b Magnetic resonance-electrical impedance tomography (MR-EIT): a new technique for high resolution conductivity imaging *2nd EPSRC Engineering Network Meeting: Biomedical Applications of EIT (University College, London)*
- Eyüboğlu B M, Birgül Ö and İder Y Z 2001 A dual modality system for high resolution-true conductivity imaging *XI Int. Conf. on Electrical Bio-Impedance (Oslo, Norway)* pp 409–13
- Eyüboğlu B M, Brown B H and Barber D C 1989 Limitations to sv determination from apt images *Proc. IEEE EMBS Conf. (Seattle, USA)* pp 442–3
- Eyüboğlu B M and Pilkington T C 1993 Comments on distinguishability in electrical impedance tomography *IEEE Trans. Biomed. Eng.* **40** 1328–30
- Eyüboğlu B M, Köksal A and Demirbilek B M 2000a Distinguishability analysis of an induced current EIT system using discrete coils *Phys. Med. Biol.* **45** 1997–2009
- Eyüboğlu B M, Reddy R and Leigh J S 1998 Imaging electrical current density using nuclear magnetic resonance *Elektrik Turkish J. Electr. Eng. Comput. Sci.* **6** 201–14
- Eyüboğlu B M, Reddy R and Leigh J S 2002 Magnetic resonance-electrical impedance tomography *Patent* US6,397,095 B1, provisional patent application on 1 Mar 1999
- Freeston I L and Tozer R C 1995 Impedance imaging using induced currents *Physiol. Meas.* **16** A257–66
- Frerichs I 2000 Electrical impedance tomography (EIT) in applications related to lung and ventilation: a review of experimental and clinical activities *Physiol. Meas.* **21** R1–R21
- Gençer N G, İder Y Z and Williamson S J 1997 Electrical impedance tomography: Induced-current imaging achieved with a multiple coil system *IEEE Trans. Biomed. Eng.* **43** 139–49
- Gisser D G, Isaacson D and Newell J C 1988 Theory and performance of an adaptive current tomography system *Clin. Phys. Physiol. Meas.* **9** A35–A41
- Gonçalves S, de Munck J C, Heethaar R M, Lopes da Silva F H and van Dijk B W 2000 The application of electrical impedance tomography to reduce systematic errors in the eeg inverse problem—a simulation study *Physiol. Meas.* **21** 379–93
- İder Y Z and Birgül Ö 1998 Use of magnetic field generated by the internal distribution of injected currents for electrical impedance tomography (mr-eit) *Elektrik Turkish J. Electr. Eng. Comput. Sci.* **6** 215–25
- İder Y Z, Eyüboğlu B M, Kuzuoğlu M, Leblebicioğlu K, Baysal U, Çağlar B K and Birgül Ö 1995 A method for comparative evaluation of EIT algorithms using a standard data set *Physiol. Meas.* **16** A227–36
- İder Y Z and Müftüleri L T 1995 Use of mri for measuring ac internal currents of eit: a feasibility study *Proc. IXth Int. Conf. on Electrical Bio-Impedance* pp 420–2
- İder Y Z and Müftüleri L M 1997 Measurement of ac magnetic field distribution using magnetic resonance imaging *IEEE Trans. Med. Imaging* **16** 617–22
- Isaacson D 1986 Distinguishability of conductivities by electric current computed tomography *IEEE Trans. Med. Imaging* **5** 91–5
- Khang H S, Lee B I, Oh S H, Woo E J, Lee S Y, Cho M H, Kwon O, Yoon J R and Seo J K 2002 J-substitution algorithm in magnetic resonance electrical impedance tomography (mreit): phantom experiments for static resistivity images *IEEE Trans. Med. Imaging* **21** 695–702
- Köksal A and Eyüboğlu B M 1995 Determination of optimum injected current patterns in electrical impedance tomography *Clin. Phys. Physiol. Meas.* **16** A99–A109
- Köksal A, Eyüboğlu B M and Demirbilek M 2002 A quasi-static analysis for a class of induced-current EIT systems using discrete coils *IEEE Trans. Med. Imaging* **21** 688–94
- Korjenevsky A, Cherepenin V and Sapetsky S 2000 Magnetic induction tomography: experimental realization *Physiol. Meas.* **21** 89–94
- Kwon O, Lee J-Y and Yoon J R 2002b Equipotential line method for magnetic resonance electrical impedance tomography *Inverse Prob.* **18** 1089–100
- Kwon O, Woo E J, Yoon J R and Seo J K 2002a Magnetic resonance electrical impedance tomography (mreit): Simulation study of *j*-substitution algorithm *IEEE Trans. Biomed. Eng.* **49** 160–67
- Liang Z P 1996 A model-based method for phase unwrapping *IEEE Trans. Med. Imaging* **15** 893–7
- Maudsley A A, Simon H E and Hilal S K 1984 Magnetic field measurement by NMR imaging *J. Phys. E: Sci. Instrum.* **17** 216–20
- Mikac U, Demsar F, Beravs K and Sersa I 2001 Magnetic resonance imaging of alternating electric currents *Magn. Reson. Imaging* **19** 845–56
- Morucci J P and Rigaud B 1996 Bioelectrical impedance techniques in medicine: Part III. Impedance imaging, medical applications *Crit. Rev. Biomed. Eng.* **24** 655–77

- Özbek O 2002 Imaging current density distribution using 0.15t magnetic resonance tomography *MSc Thesis* Middle East Technical University
- Özbek O, Birgül Ö, Eyüboğlu B M and İder Y Z 2001 Imaging electrical current density using 0.15 tesla magnetic resonance imaging system *Proc. IEEE EMBS 23th Annual Conf. CD-ROM (Istanbul, Turkey)*
- Özdemir M and Eyüboğlu B M 2002 Novel fast reconstruction algorithm for magnetic resonance electrical impedance tomography *Proc. Biyomut 8th Annual Conf. (CD-ROM) (Istanbul, Turkey)*
- Rigaud B and Morucci J P 1996 Bioelectrical impedance techniques in medicine: Part III. Impedance imaging, general concepts and hardware *Crit. Rev. Biomed. Eng.* **24** 467–588
- Scott G C, Joy M L G, Armstrong R L and Hankelman R M 1991 Measurement of non-uniform current density by magnetic resonance *IEEE Trans. Med. Imaging* **10** 362–74
- Scott G C, Joy M L G, Armstrong R L and Hankelman R M 1992 Sensitivity of magnetic resonance current density imaging *J. Magn. Reson.* **97** 235–54
- Scott G C, Joy M L G, Armstrong R L and Hankelman R M 1995 Rotating frame rf current density imaging *Magn. Reson. Med.* **33** 355–69
- Van Burik M J and Peters M J 2000 Estimation of the electric conductivity from scalp measurements: Feasibility and application to source localization *Clin. Neurophysiol.* **111** 1514–21
- Wexler A, Fry B and Neuman M R 1985 Impedance-computed tomography algorithm and system *Appl. Opt.* **24** 3985–92
- Woo E J, Soo Y L and M C W 1994 Impedance tomography using internal current density distribution measured by nuclear magnetic resonance *Proc. SPIE* **2299** 377–85
- Zhang 1992 Electrical impedance tomography based on current density imaging *MSc Thesis* University of Toronto